J. Fluid Mech. (1998), *vol.* 369, *pp.* 301–331. Printed in the United Kingdom

On the impulsive blocking of a vortex–jet

By J. A. LEE[1], O. R. BURGGRAF[2] AND A. T. CONLISK[1]

[1]Department of Mechanical Engineering, The Ohio State University, Columbus, OH 43210-1107, USA

[2] Department of Aerospace Engineering, Applied Mechanics and Aviation, The Ohio State University, Columbus, OH 43210-1107, USA

(Received 16 September 1997 and in revised form 27 March 1998)

In this paper we consider the flow field within and around a vortex as it 'collides' with a thin plate at a right angle to its axis of rotation. We show that based solely on inviscid flow theory, vorticity in the core of the vortex is redistributed significantly. The main cause of this redistribution is the presence of axial flow within the vortex; we call this vortical structure which contains axial flow a vortex–jet. In this work we show that when the axial velocity within the vortex is toward the plate, vorticity is redistributed radially outward from the core resulting in a significant reduction in the axial vorticity there; the vortex is said to 'bulge' reflecting an increase in the nominal vortex core radius. A by-product of this interaction is that the suction peak amplitude caused by the presence of the vortex rapidly decreases and the pressure soon returns to a quasi-steady distribution. On the other hand, when the axial velocity within the vortex is directed away from the surface, the suction peak persists and the vortex core radius decreases. The numerical results were validated by comparison with an analytical solution for a sinusoidal vortex jet. Analytical solutions were also derived for the initial and final states of a pure jet; the numerical results are strongly supported by the analysis. In addition, all of these results are consistent with experiments, and their relevance to the interaction between a tip vortex and a helicopter airframe is also discussed.

1. Introduction

The interaction of regions of concentrated and large vorticity with solid boundaries is a problem which has received much attention in the past 10–15 years. Problems of this nature occur when a well-defined vortex structure approaches a solid surface. In two dimensions there is a large existing literature on the subject of vortex flows and several reviews have been published on various aspects of vortex motions (Rockwell & Naudascher 1979; Rockwell 1983, 1998; Saffman & Baker 1979; Sarpkaya 1989). Most of the work described in these reviews investigates the situation where the path of the vortex is nearly parallel to the solid surface (Tucker & Conlisk 1992).

Considerably less work of an analytical and computational nature has been devoted to the three-dimensional interaction which occurs when a vortex impacts or collides with a surface at an oblique angle; in the present work we consider the situation where the collision angle is 90°. Much of the work on this problem in recent years has been done in the context of helicopter interactional aerodynamics (Affes *et al.* 1993; Kim & Komerath 1995; Liou, Komerath & McMahon 1990 among many others) and in the area of blade–vortex interactions (Marshall & Yalamanchilli 1994; see the

reviews of McCroskey (1995), Conlisk (1997), and Yu (1995) for current references to the BVI problem).

The purpose of this work is to demonstrate the inviscid nature of the decay of vorticity in the interaction of a vortex (i.e. a vortex–jet) as it collides with a body. The motivation for this work has been the analysis and computation of the interaction between a helicopter rotor and a model airframe; however, the results are intended to have much wider application. This problem is of special interest due to the fact that significant pressure loads generated on the body increase in intensity as a vortex approaches a surface. These short-time and short-length-scale suction peaks result from the development of an adverse pressure gradient due to the vortex above the surface and previous work by Affes *et al.* (1993) has shown that the suction peak on the top of a cylinder reaches a maximum as a vortex approaches before reducing in amplitude to its effectively steady value in a very short period of time. The pressure loads induced by these suction peaks may result in radiated noise and fatigue loading on the airframe.

A tip vortex shed from a wing is known to possess a significant velocity directed along its axis (Batchelor 1964) and it is this component which has a major effect on the interaction of the vortex with a downstream body. We denote this type of vortex with axial flow a 'vortex–jet' since it possesses characteristics typical of both vortices and jets. This problem has been motivated by certain features seen when a vortex shed from a helicopter rotor blade strikes an airframe. As mentioned above, we consider the case where a vortex is cut by a thin plate which is instantaneously inserted into the flow at a 90° angle to the axis of rotation of the vortex. In the case where the axial velocity in the vortex is directed towards the solid boundary, the condition that the axial flow in the vortex core must be brought to zero at the wall causes the vortex to bulge in the sense that its core becomes larger. In the case where the axial velocity in the vortex is directed away from the solid boundary, the vortex core is seen to thin locally. This phenomenon of vortex bulging and thinning has been observed in experiments by Liou *et al.* (1990) and in the later experiments described by Kim & Komerath (1995). The bulging had originally been calculated by Lee *et al.* (1995) for the problem considered here.

Figure 1 (R. Mahalingham 1997, personal communication, based on the experimental data of Kim & Komerath 1995) depicts the measured pressure distribution around a model airframe at two rotor phase angles, $\Psi = 180° + 90°$ and $\Psi = 180° + 150°$. The rotor phase angle is a time-like variable which measures the angle between the rotor and the generators of the airframe. For example, a rotor angular speed of 1050 r.p.m. corresponds to a physical time of 0.16 ms per degree of rotor phase angle, hence the time interval corresponding to 12° represents a total time of 1.9 ms. On figure 1(*a*) it is seen that the vortex has apparently 'broken' into two pieces which is indicated by the fact that there are two suction peaks on the airframe denoted by the very dark spots signifying a negative pressure coefficient. At a later time it is noted that there is a single region of low pressure located at a cylinder azimuth of about −80°; the cylinder azimuth is measured from the top of the airframe. On this side of the airframe the axial flow in the core of the vortex is directed away from the surface and it is clear that the suction peak is still very strong. On the other side of the airframe where the axial velocity in the core of the vortex is directed toward the wall, no evidence of a strong vortex is seen. This behaviour of the pressure distribution can be explained on the basis of the present work.

Another view of the same phenomenon is provided in previous work done in this area by Affes *et al.* (1993) in which experimental data (Brand, McMahon & Komerath) are compared to a simplified model for the interaction between a vortex and a model

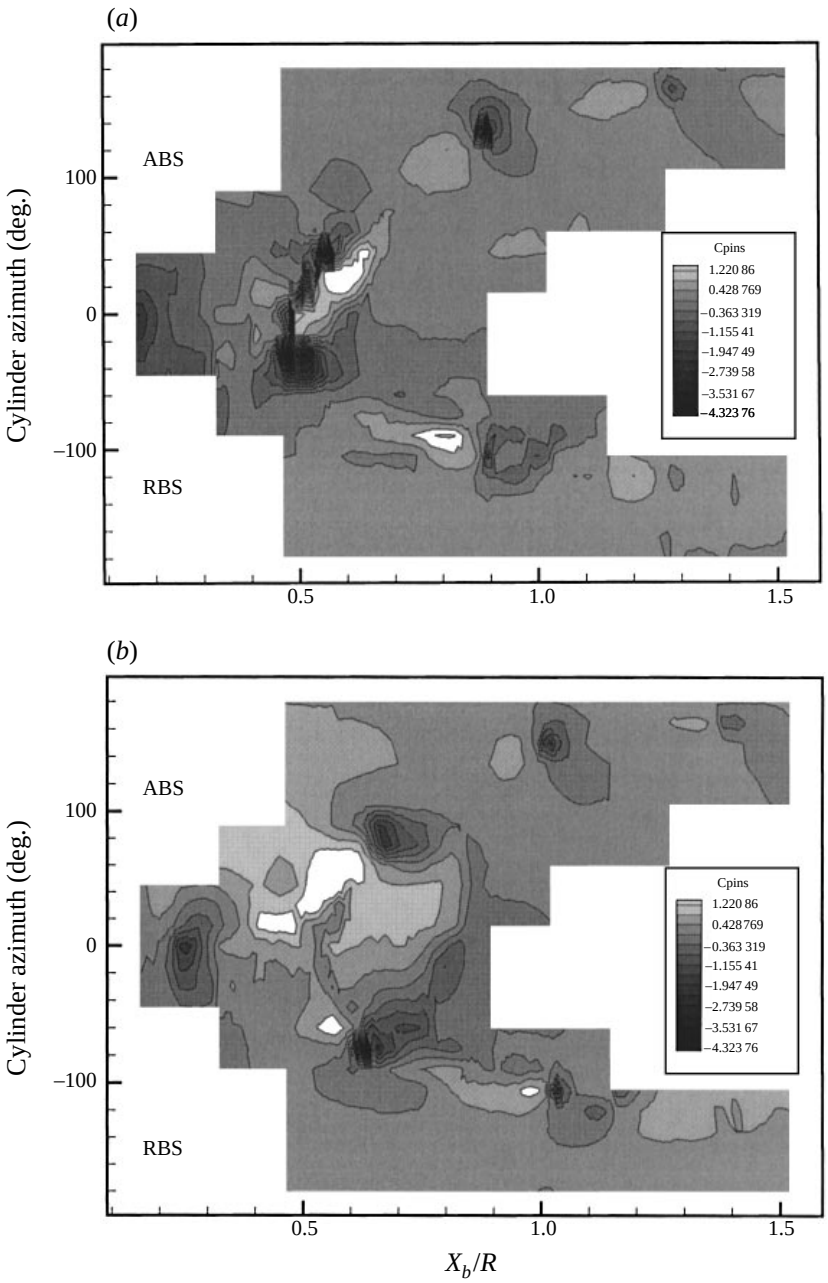

FIGURE 1. (*a*) Pressure distribution around a model airframe (R. Mahalingam 1997 personal communication) at $\Psi = 180^\circ + 90^\circ$ showing that a tip vortex has apparently broken into two separate pieces. (*b*) Pressure distribution at $\Psi = 180^\circ + 150^\circ$ showing the differences exhibited on the advancing (ABS) and retreating sides (RBS) of the airframe. On the advancing side the axial velocity in the core of the vortex is directed toward the surface and on the retreating side it is directed away from the surface. X_b/R measures distance along the airframe in the forward flight direction.

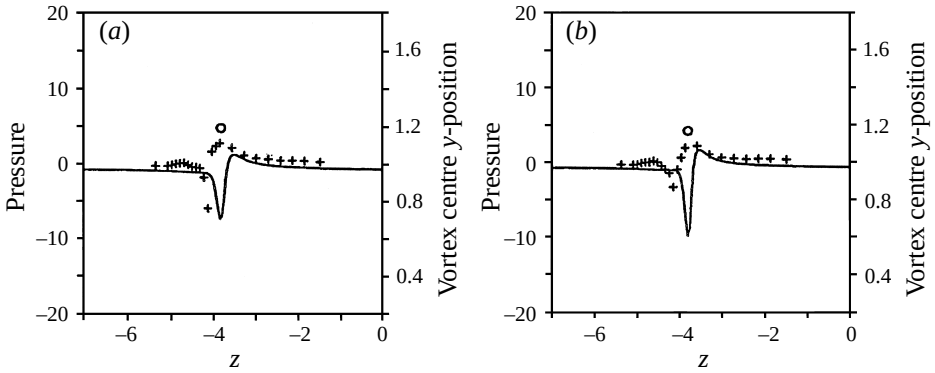

FIGURE 2. Pressure distribution along top of airframe for (*a*) $\Psi = 180° + 48°$ and (*b*) $\Psi = 180° + 54°$. From Affes *et al.* (1993). The circle denotes the vortex position.

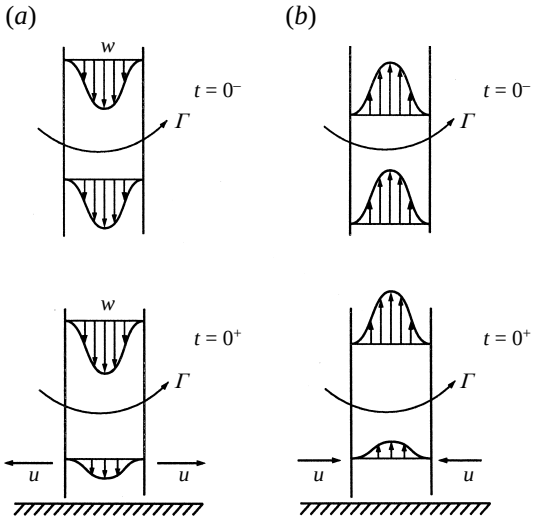

FIGURE 3. Vortex normal to a plane wall: (*a*) axial inflow; (*b*) axial outflow.

airframe. Figures 2(*a*) and 2(*b*) show the experimental and computational values for the pressure along the top of the airframe for $\Psi = 48°$ and $\Psi = 54°$ respectively; the crosses (+) are the experimental values. The rotor speed is 2100 r.p.m. It can be seen from this figure that the amplitude of the experimental suction peak on the top of the airframe decreases substantially from $\Psi = 180° + 48°$ to $\Psi = 180° + 54°$. Note that the computational model used by Affes *et al.* (1993) does not predict the relaxation of the pressure which we believe is associated with vorticity redistribution because the model does not account for modification of the vortex core nor for axial flow within the vortex.

The helicopter aerodynamics problem of interest is complicated and in an effort to understand the results of the experiments of Kim & Komerath (1995), a simplified model for the collision of a tip vortex with a solid boundary is developed. Consider an already existing, infinitely long vortex with core radius a_v, circulation Γ^*, and axial velocity w^*. At time $t^* = 0$, the vortex is instantaneously split by a plane wall normal to the axis of the vortex. Alternatively, the abrupt blocking of the jet might

be viewed as the near-axisymmetric closing of an iris-diaphragm as in some cameras. The problem is to determine the fluid behaviour for time $t^* > 0$, with particular interest in the behaviour of the pressure, swirl velocity, and the axial vorticity. For convenience, the problem is formulated in cylindrical-polar coordinates (r^*, θ, z^*) with the axis of the vortex coincident with the z-axis. The physical problem of interest is depicted on Figure 3(a) for the case where the axial velocity in the vortex is directed toward the wall. This is the case which occurs on the advancing side of the helicopter rotor in which the rotor is travelling in the same direction as the airframe. Figure 3(b) shows the problem for the case where the axial velocity in the vortex is directed away from the wall, which occurs on the retreating side of the rotor in which the rotor is travelling in a direction opposite to the flight velocity.

We have termed the interaction of the rotor-tip vortex with the airframe a vortex-surface collision and at this point it is necessary to define more precisely what is meant by that term. In the present work we consider the case where the radial scale of the vortex is much smaller than the body scale although this is not essential for the definition to be valid. To consider the more general situation where a patch of high vorticity of any shape may be affected by the presence of a body, we define the collision process as follows. A vortex–surface 'collision' is defined as the physical process in which the core structure of the vortex defined as a specified region of large vorticity surrounded by irrotational fluid is substantially and most often permanently altered. The primary cause of the collision is the axial flow in the core of the vortex; when the axial flow is directed toward the surface, the flow is 'blocked' and the vorticity originally in the core is redistributed outward forming a shell of concentrated vorticity surrounding the central portion of the vortex which is no longer rotational. When the axial velocity is directed away from the wall the flow is also 'blocked' but the vorticity in the core is redistributed inward toward the central portion of the vortex. Note that this definition of a 'collision' excludes the situation where a vortex grazes the surface of a body and the vortex core flow is essentially unaffected by the interaction.

As mentioned before, the present work is meant to have much wider applications than to just the rotorcraft problem. For example, the present analysis should describe the qualitative features of the blade–vortex interaction problem as well as the vortex buffet problem with only minor adjustments to physical parameters and initial conditions. In addition, the qualitative features of the results in this work are not expected to depend substantially on the angle at which the vortex is cut.

In the next section, the formulation of the problem is given. This is followed by the derivation of an analytical solution for a vortex in which the axial and radial velocities are independent of time. This solution exhibits many of the features of the full nonlinear problem. In addition, analytical solutions for the initial and final flow conditions for a pure jet have been derived by the second author and are presented in the Appendix. These analytical solutions for the pure jet strongly confirm the accuracy of the numerical solution.

2. Formulation

The governing equations are taken to be the axisymmetric and incompressible Euler equations; these equations are sufficient to illustrate the basic physical phenomena. All length scales are non-dimensionalized by the initial vortex core radius a_v, and all velocities are non-dimensionalized by the vortex–jet velocity w_0. With a * denoting

the dimensional variables, the non-dimensional variables are given as

$$t = \frac{t^* w_0}{a_v}, \quad r = \frac{r^*}{a_v}, \quad z = \frac{z^*}{a_v}, \quad \Gamma = \frac{\Gamma^*}{w_0 a_v},$$

$$u = \frac{u^*}{w_0}, \quad v = \frac{v^*}{w_0}, \quad w = \frac{w^*}{w_0},$$

with the non-dimensional pressure defined as

$$p = \frac{p^*}{\rho w_0^2}. \tag{1}$$

Here Γ^* is the circulation and ω^* is the azimuthal vorticity. In dimensionless form, the unsteady, axisymmetric Euler equations in cylindrical-polar coordinates (r, θ, z), with velocity components $(u, v, w) = (v_r, v_\theta, v_z)$, are given in dimensionless form as

$$\frac{\partial u}{\partial t} + u\frac{\partial u}{\partial r} + w\frac{\partial u}{\partial z} - \frac{v^2}{r} = -\frac{\partial p}{\partial r}, \tag{2}$$

$$\frac{\partial v}{\partial t} + u\frac{\partial v}{\partial r} + w\frac{\partial v}{\partial z} + \frac{uv}{r} = 0, \tag{3}$$

$$\frac{\partial w}{\partial t} + u\frac{\partial w}{\partial r} + w\frac{\partial w}{\partial z} = -\frac{\partial p}{\partial z}. \tag{4}$$

The continuity equation in cylindrical-polar coordinates for incompressible flow is given by

$$\frac{1}{r}\frac{\partial (ru)}{\partial r} + \frac{\partial w}{\partial z} = 0. \tag{5}$$

The numerical domain of solution is now $0 \leqslant r \leqslant R$ and $0 \leqslant z \leqslant L$.

The vorticity vector is defined as $\boldsymbol{\omega} = \nabla \times \boldsymbol{u}$ with the azimuthal and axial components denoted by ω and ξ. It should be noted that there exists a radial component of vorticity $-\partial v/\partial z$; however it is not required in this formulation. The azimuthal and axial components of vorticity are defined by

$$\omega = \frac{\partial u}{\partial z} - \frac{\partial w}{\partial r}, \quad \xi = \frac{1}{r}\frac{\partial}{\partial r}(rv). \tag{6}$$

In the present work we assume that the flow is axisymmetric and in this situation, rather than solve equations (2)–(5) in their present forms, it is simpler to replace the velocity components (u, v, w) with the vorticity (ω), and the stream function (Ψ). Equation (5) is satisfied by the existence of a stream function, Ψ, which is defined by the radial and axial velocity components as

$$u = -\frac{1}{r}\frac{\partial \Psi}{\partial z}, \tag{7}$$

$$w = \frac{1}{r}\frac{\partial \Psi}{\partial r}. \tag{8}$$

In terms of the stream function, equation (6) yields

$$\omega = -\frac{\partial}{\partial z}\left(\frac{1}{r}\frac{\partial \Psi}{\partial z}\right) - \frac{\partial}{\partial r}\left(\frac{1}{r}\frac{\partial \Psi}{\partial r}\right) = -\frac{1}{r}\mathrm{D}^2\Psi, \tag{9}$$

and equation (3) for the circulation function ($\Omega = rv$) becomes

$$\frac{\partial \Omega}{\partial t} + u\frac{\partial \Omega}{\partial r} + w\frac{\partial \Omega}{\partial z} = 0. \tag{10}$$

The inviscid axisymmetric azimuthal vorticity transport equation is found by combining the momentum equations (2) and (4) (thus eliminating pressure) and is given by

$$\frac{\partial \omega}{\partial t} + u\frac{\partial \omega}{\partial r} + w\frac{\partial \omega}{\partial z} - \frac{u\omega}{r} - 2\frac{v}{r}\frac{\partial v}{\partial z} = 0, \tag{11}$$

with u and w given by equations (7) and (8). Equations (9), (10) and (11) are solved simultaneously for the three unknowns Ψ, $v = \Omega/r$ and ω.

In the following we formulate the boundary conditions for the case where the axial velocity is directed toward the wall, assumed to be $z = 0$. Four boundary conditions are needed for the elliptic equation (9). It is expected that the influence of the wall is not felt at $z = L$ (precisely true only in the limit as L approaches infinity), and hence the following Dirichlet boundary condition may be used:

$$\Psi = \int_0^R r w_I \mathrm{d}r \quad \text{on} \quad z = L, \tag{12}$$

where w_I is a prescribed function of r. For time $t > 0$, the axial velocity w must be zero on the wall and hence

$$\Psi = 0 \quad \text{on} \quad z = 0; \tag{13}$$

similarly, on $r = 0$, u must be zero, yielding

$$\Psi = 0 \quad \text{on} \quad r = 0. \tag{14}$$

The axial velocity vanishes as $r \to \infty$ and so

$$\frac{\partial \Psi}{\partial r} = 0 \quad \text{on} \quad r = R \tag{15}$$

is the appropriate outer boundary condition provided R is sufficiently large.

The hyperbolic equations (11) and (10) also require boundary conditions specified on the inflow boundary $z = L$. For the vorticity transport equation (11), we assume that the vorticity at $z = L$ does not change from its initial condition for all time, which corresponds to a constant inflow (or outflow) of azimuthal vorticity. This is valid as long as the effects of the wall are not felt at $z = L$. In this case, the circulation function, equation (10), at $z = L$ also remains unchanged from its initial condition.

The pressure is obtained by integrating equations (2) and (4) with the reference pressure taken at $r = R$, $z = 0$. That is, equation (4) is solved on $r = R$, with the reference pressure being $p(R, 0, 0) = 0$. Equation (2) is used to solve the pressure elsewhere with the reference pressure being $p(R, z, t)$. For example, if equation (4) is expressed in conservative form, then the pressure on $r = R$ is given by

$$p(R, z, t) = -\int_0^z \left(\frac{\partial w}{\partial t} + \frac{1}{r}\frac{\partial}{\partial r}(ruw) + \frac{\partial}{\partial z}\left(w^2\right) \right) \mathrm{d}z \tag{16}$$

and integrating equation (2) similarly yields

$$p(r, z, t) = \int_r^R \left(\frac{\partial u}{\partial t} + \frac{1}{r}\frac{\partial}{\partial r}\left(ru^2\right) + \frac{\partial}{\partial z}(uw) - \frac{v^2}{r} \right) \mathrm{d}r + p(R, z, 0), \tag{17}$$

where we have assumed that R is large enough so that $p(R, z, t) = p(R, z, 0)$.

3. Numerical methods

The vorticity–stream function representation of the Euler equations given in the previous section actually contain two separate types of equations: equation (9) is a two-dimensional second-order elliptic equation, whereas equations (10) and (11) are two-dimensional unsteady nonlinear first-order hyperbolic equations. This suggests that the implementation of at least two different numerical schemes is necessary to solve the system of equations. Equation (9) can be solved easily using the standard finite-difference methods and Gauss–Seidel iteration. The standard numerical method for solving the hyperbolic equations (10) and (11) is the method of characteristics. However, the programming of the method of characteristics is much more difficult than the programming of finite-difference methods, especially for problems involving a set of simultaneous two-dimensional nonlinear first-order equations. For this reason, numerical methods chosen for the solution of equations (10) and (11) utilize finite-difference methods. To significantly reduce the amount of computation time required, the multigrid method is employed in the solution of equation (9).

The numerical solution to equation (9) subject to boundary conditions (12)–(15) is calculated using a standard finite-difference scheme. The differential equation (9) is discretized in the (r, z)-plane with uniform fixed grid spacing in both coordinates. Let i be the spatial index in the radial direction which varies from 0 to M and j be the spatial index in the axial direction which varies from 0 to N. The total number of gridpoints is $(N+1) \times (M+1)$. The grid spacings are $\Delta r = R/M$ and $\Delta z = L/N$, where R and L are the lengths of the computational domain in the r- and z-directions respectively.

Second-order central differences are used for the spatial derivatives in equation (9) and these are

$$\left.\frac{\partial \Psi}{\partial r}\right|_{i,j} = \frac{\Psi_{i+1,j} - \Psi_{i-1,j}}{2\Delta r} + O(\Delta r)^2, \tag{18}$$

$$\left.\frac{\partial^2 \Psi}{\partial r^2}\right|_{i,j} = \frac{\Psi_{i+1,j} - 2\Psi_{i,j} + \Psi_{i-1,j}}{(\Delta r)^2} + O(\Delta r)^2, \tag{19}$$

with similar discretization in the z-direction. Accuracy is improved near $r = 0$ by using a fourth-order central difference approximation for $\partial \Psi / \partial r$ which is given by

$$\left.\frac{\partial \Psi}{\partial r}\right|_{i,j} = \frac{-\Psi_{i+2,j} + 8\Psi_{i+1,j} - 8\Psi_{i-1,j} + \Psi_{i-2,j}}{12\Delta r} + O(\Delta r)^4, \tag{20}$$

which yields truncation error $O(\Delta r)^3$ in equation (9) when $r \sim \Delta r$ and is valid for $i = 2, \ldots, M-2$, and $j = 0, \ldots, N$. Also for the points $i = 1$ and $i = M-1$ adjacent to the boundaries, fourth-order sloping difference formulas for $\partial \Psi / \partial r$ are used.

The difference equation is solved using a standard Gauss–Seidel point-iterative scheme with successive over-relaxation (SOR) coupled with a multi-grid scheme to accelerate convergence. After each iteration of the system of equations is calculated, relaxation is applied with the relaxation parameter of 1.8 used in the present calculations. The process is repeated until the relative convergence test

$$\max\left(\left|1 - \frac{\Psi_{i,j}^{n+1}}{\Psi_{i,j}^{n}}\right|\right) < \epsilon, \tag{21}$$

is satisfied for a criterion of $\epsilon = 10^{-7}$. If the convergence test given in equation (21) is satisfied, then the computed values of Ψ are used to calculate the velocities u and w as shown below, and the other two governing equations (10) and (11) are solved using a second-order predictor-corrector method in time, and second-order upwind differencing in space and all variables are saved at that time level. Otherwise, the iteration is continued.

The meridional flow velocities u and w are calculated from equations (7) and (8) using standard fourth-order finite differences. Fourth-order approximations are used in order to retain accuracy for $r \sim \Delta r$, and the equations are similar to those given above for $\partial \Psi / \partial r$.

The pressure is found through the numerical integration of equations (16) and (17) using a second-order-accurate trapezoidal rule. The unsteady terms are calculated using a three-point second-order backward difference in time, and are given by

$$\left.\frac{\partial u}{\partial t}\right|_{i,j}^{n} = \frac{-3u_{i,j}^{n-2} + 4u_{i,j}^{n-1} - u_{i,j}^{n}}{2\Delta t} + O(\Delta t)^2, \tag{22}$$

$$\left.\frac{\partial w}{\partial t}\right|_{i,j}^{n} = \frac{-3w_{i,j}^{n-2} + 4w_{i,j}^{n-1} - w_{i,j}^{n}}{2\Delta t} + O(\Delta t)^2, \tag{23}$$

where $n \geqslant 2$ is the current time level. For $n = 1$ central differences are used. For $n = 0$, it can be seen from equations (16) and (17) and the initial conditions given in equations (29), (30) and (31) that the only contribution to the pressure is that from the swirl velocity. All spatial derivatives used in the calculation of the pressure are standard fourth-order central differences.

The axial vorticity as defined in equation (6) is calculated using standard fourth-order-accurate finite-difference schemes such as given in equation (20). Again, fourth-order-accurate schemes are used to reduce the effect of the division by r in equation (6) which causes reduction in accuracy for $r \sim \Delta r$.

The computational procedure for solving the system of equations consisting of the stream function, the vorticity-transport equation, and the circulation function is carried out in the following order.

(1) Begin with initial distributions of u, v, w, ω, Ψ.

(2) Calculate $\omega_{i,j}^{n+1/2}$, and $v_{i,j}^{n+1/2}$ from the predictor step of the discretization of equations (10) and (11).

(3) Using the multigrid method, calculate $\Psi_{i,j}^{n+1/2}$ using $\omega_{i,j}^{n+1/2}$.

(4) Calculate the meridional flow $u_{i,j}^{n+1/2}$ and $w_{i,j}^{n+1/2}$ from $\Psi_{i,j}^{n+1/2}$ from equations (7) and (8).

(5) Calculate $\omega_{i,j}^{n+1}$, and $v_{i,j}^{n+1}$ from the corrector step.

(6) Calculate $\Psi_{i,j}^{n+1}$ using $\omega_{i,j}^{n+1}$ using the multigrid scheme.

(7) Calculate the meridional flow $u_{i,j}^{n+1}$ and $w_{i,j}^{n+1}$ from $\Psi_{i,j}^{n+1}$.

(8) Solve for the axial vorticity from equation (6) and calculate the pressure as described above.

(9) Transfer all the newly computed values to the previous time-level and go to the next time level. Repeat steps 2–9 until the desired time is reached.

The present computational scheme was tested on a model problem for which an analytical solution can be found. This problem exhibits many of the features of the full nonlinear problem and it is worthwhile to investigate this problem first.

4. The sinusoidal model problem

Consider the following initial conditions for the radial, swirl, and axial velocity components (u, v, w):

$$u = \frac{B}{r} \sin \frac{\pi r^2}{2}, \tag{24}$$

$$v = \frac{A}{r} \sin \frac{\pi r^2}{2}, \tag{25}$$

$$w = -Bz\pi \cos \frac{\pi r^2}{2}, \tag{26}$$

where $A = \Gamma/2\pi$, B is a constant which controls the magnitude and direction of the meridional flow and is related to the volume flow rate Q through the plane $z = L$ by $B = -Q/2\pi L$. Thus for $B > 0$, the axial velocity w is directed toward the wall, and for $B < 0$, w is directed away from the wall.

The domain of this problem is $0 \leqslant r \leqslant 1$ and $0 \leqslant z \leqslant L$ where L is the length of the domain in the axial direction. Note that an analytical solution exists for $r \geqslant 1$; however, it is not presented here as the validity of the computational scheme can be evaluated strictly from the analytical solution generated within the vortex core.† Also note that the boundary conditions in this problem are the same as those given in the previous Section.

The second author has shown that if we assume u and w to be independent of time, then the circulation function which satisfies equation (10) can be used to solve the time-dependent swirl flow and the swirl is given by

$$v = \frac{2A}{r} \frac{e^{\pi Bt} \tan(\frac{1}{4}\pi r^2)}{e^{2\pi Bt} + \tan^2(\frac{1}{4}\pi r^2)}. \tag{27}$$

From the swirl velocity, the axial vorticity ξ can be found from equation (6) and is given by

$$\xi = \pi A e^{\pi Bt} \frac{e^{2\pi Bt}\cos^2(\frac{1}{4}\pi r^2) - \sin^2(\frac{1}{4}\pi r^2)}{[e^{2\pi Bt}\cos^2(\frac{1}{4}\pi r^2) + \sin^2(\frac{1}{4}\pi r^2)]^2}. \tag{28}$$

Since the meridional flow is taken to be steady and the swirl velocity is independent of z for all time t, the azimuthal component of vorticity is also independent of time. This can be seen by substituting expressions (24), (26), and (27) into the vorticity transport equation (11), where the result is $\partial\omega/\partial t = 0$.

The solution for the swirl velocity and the azimuthal vorticity are illustrative of the more general solutions to the full nonlinear problem. Note that for $B > 0$ the swirl velocity decreases rapidly in time at a fixed value of r; simultaneously, the axial vorticity decreases as well. This means that at fixed $r < 1$, eventually there is no swirl and no azimuthal vorticity; that is, no vortex inside $r = 1$. This is precisely what is seen in the solution for the full nonlinear problem. On the other hand, for $B < 0$, both the swirl and the azimuthal vorticity *increase* exponentially with time at a fixed value of r; again this is precisely what is seen in the full nonlinear problem.

To validate the full nonlinear algorithm, the numerical solution to this model problem is generated by using the velocities given in equations (24)–(26) as initial conditions to the computational procedure outlined in the previous section. All

† The above solution actually holds throughout the region $0 \leqslant r \leqslant \sqrt{2}$, representing swirl flow in a tube, down the axis to the end wall at $z = 0$ and back up along the tube wall at $r = \sqrt{2}$.

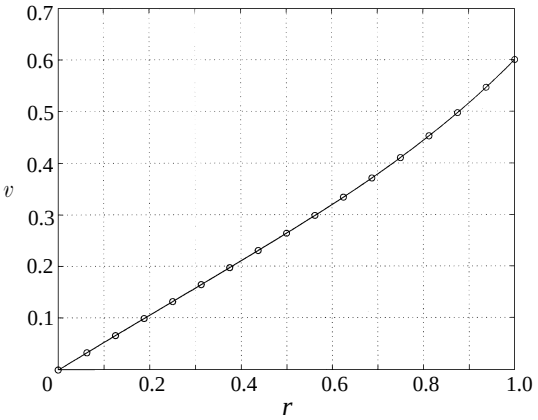

FIGURE 4. Swirl velocity distribution on the wall for the analytical case of § 4 with $A = B = 1$. ○, Numerical solution; ——, analytical solution at time $t = 0.175$.

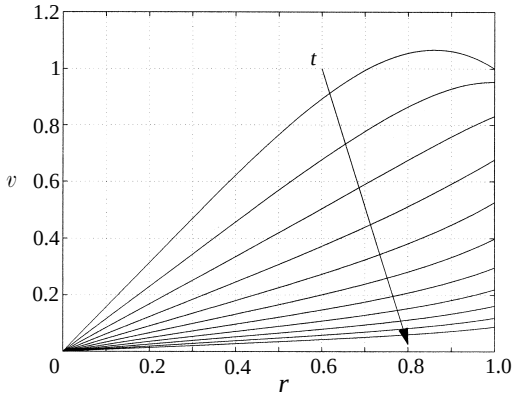

FIGURE 5. Swirl velocity distribution on the wall for the analytical case of § 4 with $A = B = a = 1$. Time ranges from 0 to 1.0 in increments of 0.1. In this and subsequent figures time increases in direction of arrow.

quantities were computed as time-dependent even though they do not in fact vary with time. Figure 4 shows the numerical solution for the swirl velocity on the wall after 700 time steps compared with the analytical solution. The numerical solution was obtained for $A = B = 1$, $\Delta t = 0.00025$, $R = L = 1$, $M = N = 64$, $\lambda = 1.8$, and $\epsilon = 10^{-7}$ and is four-digit accurate in comparison with the analytical solution. Figure 5 shows the swirl velocity for this case for successive times; note the rapid decrease in the core. This feature is characteristic of the solution to the full problem as well; coincident with this decrease in the swirl is a substantial decrease in the axial vorticity (not shown). The results of figure 5 describe the process of a vortex–surface collision as defined in the Introduction. We now proceed to the results for the full nonlinear problem.

5. Results for the full nonlinear problem

Based on the success of the computational scheme in reproducing the results for the analytical model problem, we now present results for the fully nonlinear and

unsteady problem defined in § 2. To provide a baseline for comparison of the results for the vortex flow, it is useful to consider the case where the swirl velocity is zero so that the flow is a pure jet. We present solutions first for the case of the axial flow toward the wall for both the case of the pure jet and the vortex–jet. Then we reverse the direction of the axial flow and consider the case where the axial flow is directed away from the wall.

To start the problem, we choose initial conditions corresponding to an undisturbed vortex with axial flow. The initial axial velocity distribution for this flow is taken as the simple form

$$w = w_I = -\mathrm{e}^{-r^2}, \tag{29}$$

where the negative sign denotes that the axial velocity is toward the wall. Since the jet is undisturbed at time $t = 0^-$, we set the initial radial velocity as

$$u = u_I = 0. \tag{30}$$

The initial swirl velocity distribution that is assumed to exist up to time $t = 0^-$ is taken to be a Lamb-type vortex (Lamb 1945)

$$v = v_I = \frac{\Gamma}{2\pi r}\left(1 - \mathrm{e}^{-r^2}\right), \tag{31}$$

corresponding to a decayed potential vortex with a linear swirl as $r \to 0$. Correspondingly, the initial circulation distribution is then

$$\Omega = \Omega_I = rv_I = \frac{\Gamma}{2\pi}\left(1 - \mathrm{e}^{-r^2}\right). \tag{32}$$

The initial azimuthal vorticity distribution is defined by equation (6) as

$$\omega = \omega_I = -\frac{\partial w_I}{\partial r} = -2r\,\mathrm{e}^{-r^2}. \tag{33}$$

Numerical solutions have been computed for three sets of grids corresponding to $(64)^2$, $(128)^2$, and $(256)^2$ points, for $R = L = 4$ and the results for the velocities and the vorticity for each grid were compared. It was found that sufficient spatial resolution is achieved using 128 grid points in both r and z. This was measured by requiring two-figure accuracy in the velocities; the vorticity values are slightly less accurate although two-figure accuracy was obtained at almost all points in the grid as well. Sufficient temporal accuracy is achieved using a time step of $\Delta t = 0.01$. In addition, the effects of the lengths of the computational domain in r and z on the numerical solution for the case of no swirl was tested, resulting in a 2.9% change in the azimuthal vorticity on the wall when R and L are doubled from 4 to 8. The grid spacing was held fixed at $\Delta r = \Delta z = 0.0312$ with $\Delta t = 0.01$ and the convergence criterion $\epsilon = 10^{-7}$ for these tests. All of the results presented here are for 128 points in both directions with $R = L = 4$, $\Delta t = 0.01$.

We have assumed that the vortex is instantaneously sliced; in reality we would expect a thin layer of vorticity to be wrapped around the leading edge of the plate. The time scale associated with the wrapping of vorticity around the leading edge is $t_w \sim a_v/U$ where a_v is the vortex core radius and U is the speed of the plate. The time scale associated with the simplified interaction is $t_v \sim a_v/W$ where W is the axial velocity scale. If these time scales are sufficiently different these two phenomena will not interact. Thus if $U \gg W$ then the time scale of the wrapping is much shorter than the redistribution process. Moreover, the axial vortex lines which are deformed into the radial direction by the plate will ultimately lie parallel to the plate, and the

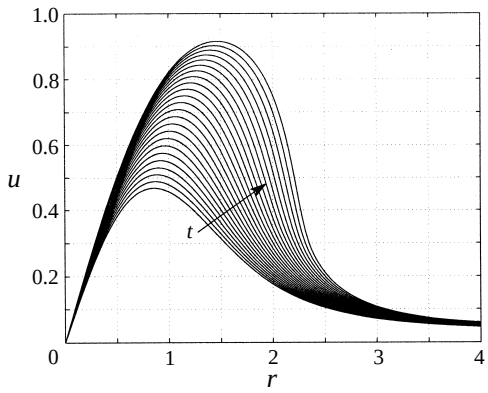

FIGURE 6. Radial velocity distribution on the wall for the pure jet with axial flow in the jet directed toward the wall. Time ranges from 0 to 2.5 in increments of 0.1.

portions on the top and bottom of the plate cancel each other since those portions have opposite-signed vorticity.

5.1. *The pure jet: axial velocity directed toward the wall*

In this section, we consider the case where $\Gamma = 0$ in equation (31), or a pure jet for the case of flow directed toward the wall. At time $t = 0$, a wall is instantaneously inserted into the flow at a right angle to the jet. In the case where the axial velocity is directed toward the wall, the resulting stagnation at the wall causes the fluid to flow radially outward locally near the wall. Analytical solutions for the limit cases $t = 0^+$ and $t \to \infty$ have been derived by the second author and are presented in the Appendix. They serve as useful comparisons for evaluating the reliability of the computational solutions.

Figure 6 shows the radial velocity on the wall as a function of time. The computed values for $t = 0^+$ compare very well with those predicted by the analytical solution presented in figure 24 of the Appendix. As time increases, the radial velocity approaches the steady state for small r, as given in § A.2 (see figure 24); indeed, the comparison is quite good up to $r \approx 1.2$ at $t = 2.5$. This indicates that for no swirl, the time scale a_v/w_0 determines the development of the steady jet flow. Outside this inner core of near steady flow, the radial velocity peaks and then falls off toward zero, with a large negative radial-velocity gradient developing as time increases. This reversal in the sign of the radial-velocity gradient suggests that the axial velocity also reverses its sign, producing upwelling in this region of large radial-velocity decay. The analytical solution for $t = 0^+$ predicts upwelling for $r > r^*$, where $r^* = 1.256\,963\cdots$. As the radial-velocity fall-off steepens, the upwelling also increases, possibly producing a local eruption of the fluid near the wall. This upwelling is coincident with the development of a region of high azimuthal vorticity, as seen in figure 7(*a*). The peak wall azimuthal vorticity increases with time, in absolute value, while moving radially outward. Note that the vorticity curves, out to about $r = 2$, coalesce to the steady-flow limit $\omega = -2r$ (see Appendix). This situation progresses until a near-discontinuity is formed and the numerical solution breaks down.

The development of this vorticity discontinuity is due to the outward propagation of the jet-core vorticity into the external region of zero vorticity. Note that in any flow with positive radial velocity that decays monotonically with increasing radius, the fluid particles must converge, since the inner particles move faster than the outer

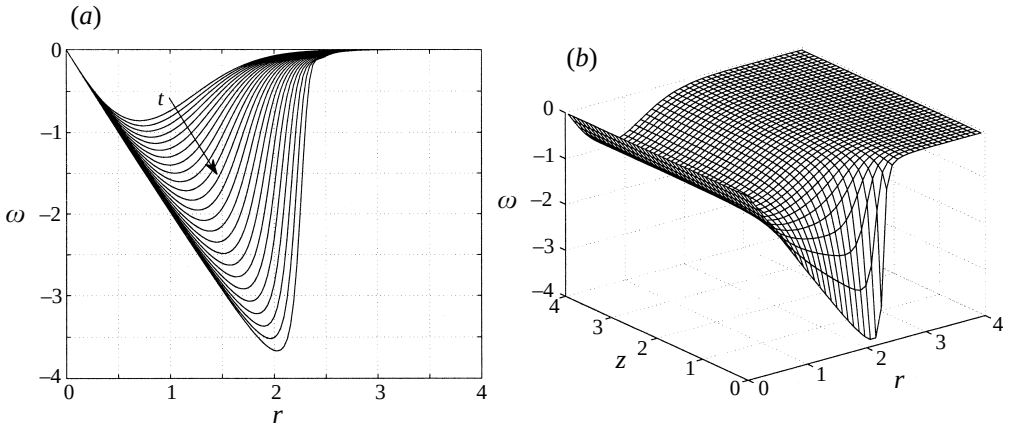

FIGURE 7. Azimuthal vorticity distribution: (*a*) on the wall for the pure jet with axial flow directed toward the wall. Time ranges from 0 to 2.5 in increments of 0.1. (*b*) Three-dimensional view at $t = 2.5$. Every third point is plotted.

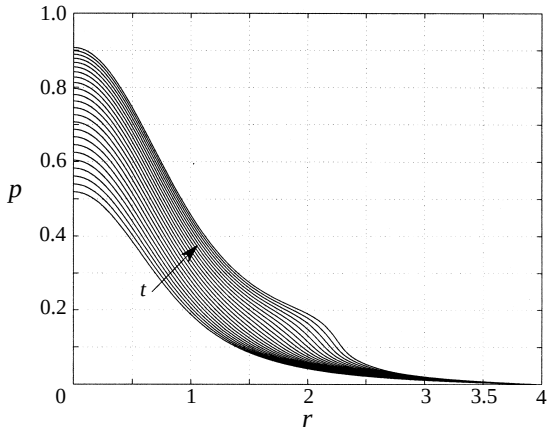

FIGURE 8. Pressure distribution on the wall for the pure jet with axial flow directed toward the wall. Time ranges from 0 to 2.5 in increments of 0.1.

ones. Hence, any property carried by the particles will become more concentrated. In the present case, the azimuthal vorticity was initially confined inside the radius of the jet, and as it is carried radially outward, the rotational fluid develops into a shell of ever decreasing thickness. An adaptive-gridding numerical scheme would be better able to treat this situation. It should also be noted that the azimuthal vorticity varies most drastically near the wall. Farther out from the wall the azimuthal vorticity field changes very little from its initial distribution. To illustrate, a three-dimensional plot of the azimuthal vorticity field at time $t = 2.5$ is shown in figure 7(*b*).

Figure 8 shows the pressure on the wall as a function of time. It can be seen that the pressure is moving toward a steady value near the axis $r = 0$ (evidenced by the clustering of curves near $r = 0$); however it has not yet reached a steady value. This is due to the fact that the pressure on the wall is only affected by the time-change of u, and the change in u with respect to r as can be seen in equation (2). Also note the outward travelling wave in the pressure which increases in magnitude as time

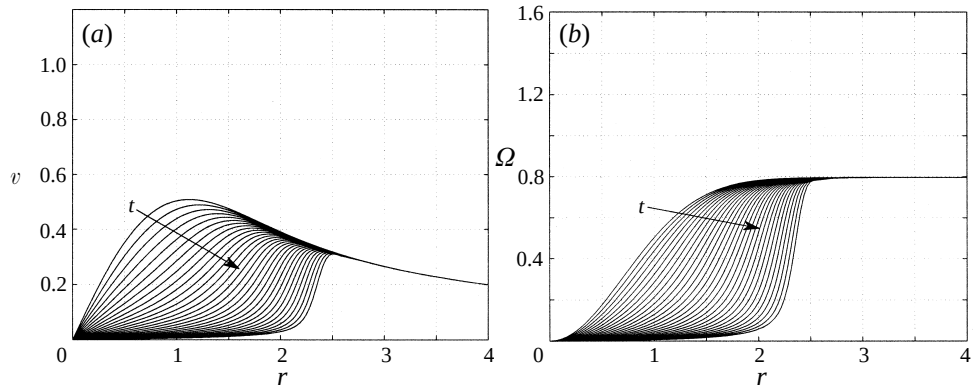

FIGURE 9. (*a*) Swirl velocity distribution on the wall for the vortex–jet with axial flow directed toward the wall ($\Gamma = 5$). Time ranges from 0 to 3.1 in increments of 0.1. (*b*) Circulation function $\Omega = rv$ on the wall.

increases. This is caused by the large radial gradient of the radial velocity which also corresponds to the presence of large azimuthal vorticity in the region near the wall.

5.2. *The vortex–jet: axial velocity directed toward the wall*

In this section, the effects of the addition of swirl velocity to the pure jet flow is investigated. Here we consider the case where the axial flow within the swirling jet is directed toward the wall. As previously stated, the only dimensionless parameter from the non-dimensionalization in § 2 is the circulation associated with the complete vortex core, Γ. In this section, we focus on the value of $\Gamma = 5$; the influence of the value of Γ is considered in the next section.

Figure 9(*a*) shows the swirl velocity on the wall as a function of time. The swirl velocity is reduced rapidly near $r = 0$, forming a growing inner core of rotationally dead air. Outside this inner core, the swirl rapidly increases to the potential vortex level. The apparent bulging of the vortex core is evident here, as the location of the peak swirl velocity is carried radially outward by the radial velocity, shown later in figure 11. Figure 9(*b*) shows the circulation on the wall as a function of time. As required by Kelvin's theorem, the circulation remains constant outside the vortex core, implying that the total vorticity is merely redistributed by convection, not destroyed. Evident here is also the rapid development of the stagnant inner core, bounded by an annular shell of vorticity, corresponding to the rise of the circulation function to its limiting value of $\Gamma/2\pi$. The evident steepening of the circulation distribution outside the inner core is caused by the decrease of radial velocity with r. It can be seen in figure 11 that the radial velocity decreases somewhat faster than $1/r$ at the outer edge of the vortex, suggesting that the inner radius of the annulus of vortex filaments moves outward faster than the outer radius, thus producing a thinning of the shell with the result that the increase of circulation across the shell occurs over ever smaller radial distances. Correspondingly, the vortex filaments are squeezed together in this narrow annulus, producing an increase in the magnitude of the axial vorticity in the shell, as is evident in figure 10.

Figure 10(*a*) shows the axial vorticity on the wall as a function of time. It can be seen in this figure that the axial vorticity on the wall decreases near $r = 0$ as time increases, and spreads radially outward with time. This behaviour can be explained as follows. From the second of equations (6) the axial vorticity is $1/r$ times the radial

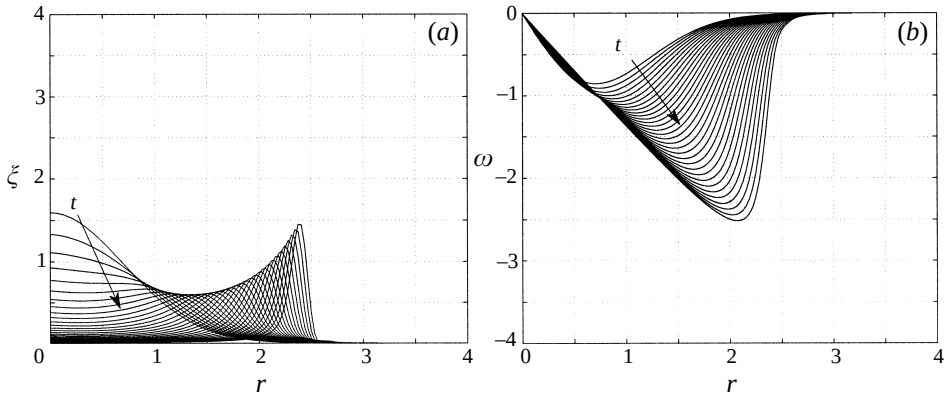

FIGURE 10. Vorticity distribution on the wall for the vortex–jet with axial flow directed toward the wall and $\Gamma = 5$. Time ranges from 0 to 3.1 in increments of 0.1. (*a*) Axial vorticity; note again the rapid decrease in the axial vorticity in the original core of the vortex. (*b*) Azimuthal vorticity distribution.

derivative of the circulation. The circulation satisfies a first-order wave-type equation so it is not surprising that the vorticity should be redistributed. Moreover, from figure 9(*b*) the circulation is approaching zero rapidly for $r \leqslant 1$ so that the axial vorticity there is small but finite as $r \to 0$. This behaviour is the main feature of the vortex–surface collision process. What was once a vortex (in the sense of a line vortex) is now locally rotationally dead, and the outer portion of the vortex which was once rotationally dead, now possesses significant axial vorticity. The original vortex has been transformed such that the high levels of axial vorticity become concentrated in a thinning annular shell at ever increasing values of r.

The azimuthal vorticity on the wall as a function of time is depicted on figure 10(*b*). Note here that the magnitude of the peak value of azimuthal vorticity on the wall first increases, then levels off, then continues to increase monotonically. In contrast, for the pure jet, the azimuthal vorticity on the wall increases in magnitude monotonically with no plateau, suggesting that this is a swirl-dominated effect. The maximum absolute value of the azimuthal vorticity in this case is only about 56% of that in the pure jet-flow case with axial inflow by time $t = 2.5$. This indicates that even though the azimuthal vorticity distribution on the wall has the same general trend as that of the jet (see figure 7*a*), the addition of swirl slows down the rate of outward travel of both the radial velocity and the azimuthal vorticity. As in the pure jet case, the azimuthal vorticity varies most drastically near the wall. Farther out from the wall the azimuthal vorticity field changes very little from its initial distribution.

Figure 11 shows the radial velocity on the wall as a function of time. Here the peak radial velocity on the wall increases, then levels off as time increases. It is seen that the magnitude of the radial velocity at time $t = 5$ is only about 70% of that in the jet case investigated in the previous subsection. The same steepening of the radial velocity curves occurs here. This fluid upwelling, as in the jet, is caused by the presence of a region of significant azimuthal vorticity as seen in figure 10(*b*).

Figure 12 shows the pressure on the wall as a function of time. Note that the pressure at time $t = 0^-$, denoted by the $*$, is due to the swirl flow only. It can be seen that the pressure jumps instantaneously at time $t = 0^+$ which is due to the insertion of the wall. Also note that the pressure is approaching a steady value especially near

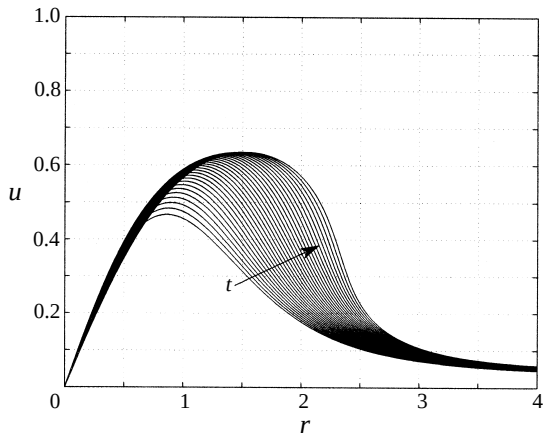

FIGURE 11. Radial velocity distribution on the wall for the vortex–jet with axial flow directed toward the wall and $\Gamma = 5$. Time ranges from 0 to 3.1 in increments of 0.1.

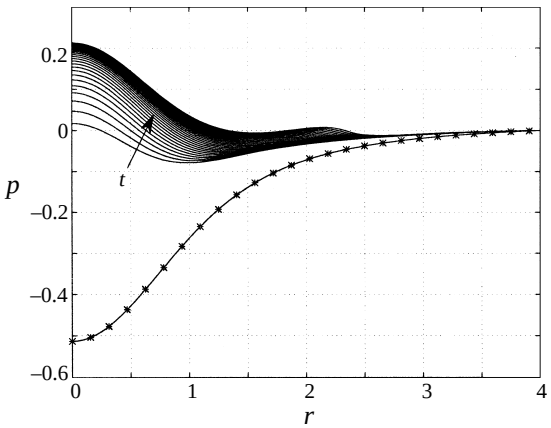

FIGURE 12. Pressure distribution on the wall for the vortex–jet with axial flow directed toward the wall ($\Gamma = 5$). Time ranges from 0 to 3.1 in increments of 0.1. The $*$ indicate the initial condition, $t = 0^-$.

$r = 0$, as evidenced by the clustering of curves at later times. Recall that the given pressure is relative to the value at $(R, 0, 0)$. This apparent near steady behaviour on the wall is due to the fact that the radial velocity is nearly steady in this region. In addition, the swirl velocity has nearly disappeared near the origin and thus its contribution to the radial momentum equation is negligible. It can also be seen that there is a secondary wave travelling radially outward. This outward travelling wave is a result of the steepening of the radial velocity profile on the wall which is indicative of a local fluid eruption. This region of adverse pressure is expected to be convected eventually outside the computational domain.

The major conclusion of the present section is that the presence of the wall forces fluid outward from the centre of the core leaving behind a core devoid of swirl and axial vorticity. Recall that this is precisely the situation illustrated by the analytical solution presented in § 4. Moreover, the pressure results provide an explanation for the reduction of the suction peak in the pressure seen on the advancing side of a helicopter as depicted on figure 1(*a*) and on the top of the airframe as seen on

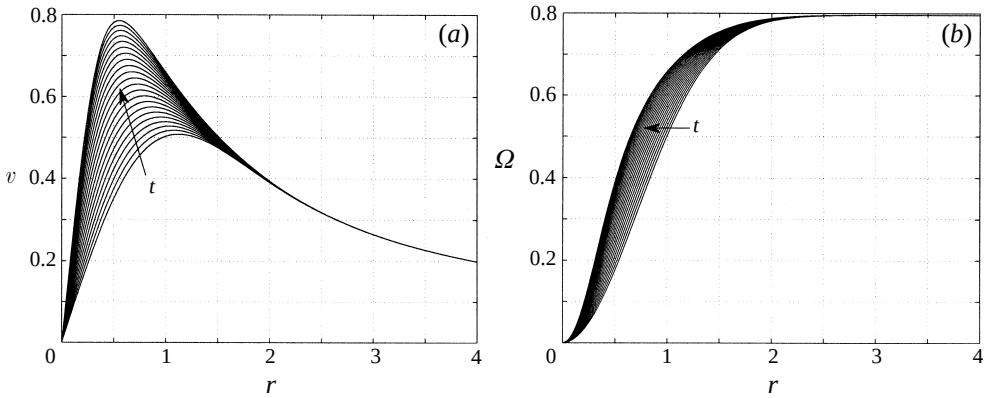

FIGURE 13. (*a*) Swirl velocity distribution on the wall for the vortex–jet with axial flow directed away from the wall ($\Gamma = 5$). Time ranges from 0 to 1.1 in increments of 0.05. (*b*) Circulation function, $\Omega = rv$ on the wall.

Figure 2(*b*). In addition, it is clear that this reduction in pressure would not occur unless there is axial velocity in the core; that is, from an inviscid point of view, there is no collision unless there is axial flow in the core of the vortex. We now move on to the case where the axial flow in the vortex is directed away from the wall.

5.3. *The vortex–jet: axial velocity directed away from the wall*

Here we consider the case where the axial velocity is directed away from the wall. The boundary condition at the wall causes the fluid to be drawn radially inward toward the axis $r = 0$. To consider this problem using the current program, we merely reverse the sign of the axial velocity. The problem then is theoretically ill-posed since we apply a boundary condition on the circulation function and the azimuthal vorticity at $z = L$, which is now a downstream boundary. In addition, the derivatives in the hyperbolic equations (10) and (11) are evaluated using an upwinding scheme in which the solution downstream always depends upon the solution upstream. In order for the axial outflow problem to be theoretically well-posed, the azimuthal vorticity corresponding to a constant radial inflow would have to be specified at $t = 0$ on the boundary at $r = R$. Even though the axial outflow problem is ill-posed, the present time-marching scheme was successful for this case over a considerable length of time.

The swirl velocity on the wall for the case of axial outflow is shown in Figure 13(*a*). It can be seen in this figure that the swirl velocity on the wall focuses as time increases. This focusing of the swirl velocity is evidence of a contraction of the vortex. During this contraction, the peak swirl velocity moves radially inward as it is convected by the radial velocity. Figure 13(*b*) shows the circulation function on the wall for the case of axial outflow. It can be seen in this figure that the circulation on the wall is convected radially inward by the radial velocity. This steepening corresponds to the fact that fluid particles are bunching up near $r = 0$, and hence the increase in circulation occurs over ever smaller radii.

Figure 14 shows the axial vorticity on the wall for the case of axial outflow. Note that the axial vorticity on the wall focuses as time increases. This focusing of the axial vorticity is caused by the contraction of the swirl velocity. Also, the axial vorticity seems to be approaching a steady value near $r = 0$, which is consistent with the behaviour of the swirl velocity profile for later times near $r = 0$.

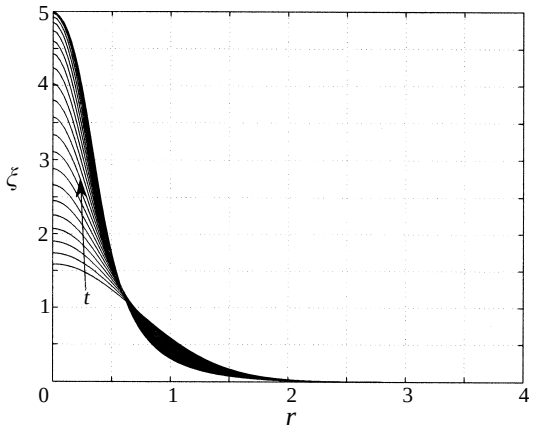

FIGURE 14. Axial vorticity distribution on the wall for the vortex–jet with axial flow directed away from the wall ($\Gamma = 5$). Time ranges from 0 to 1.1 in increments of 0.05. Note here the focusing of the vorticity near $r = 0$.

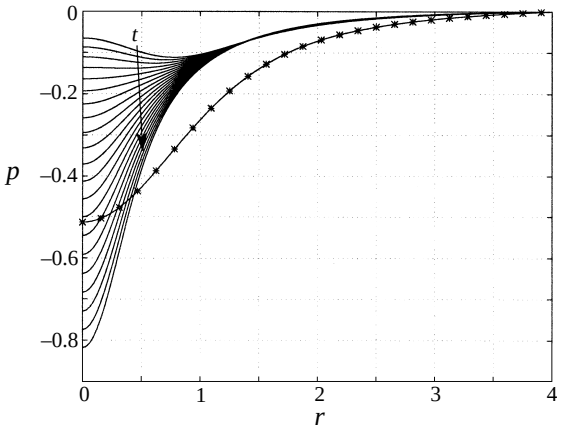

FIGURE 15. Pressure distribution on the wall for the vortex–jet with axial flow directed away from the wall for $\Gamma = 5$. Time ranges from 0 to 1.1 in increments of 0.05. The $*$ denote the pressure at $t = 0^-$.

Figure 15 shows the pressure on the wall as a function of time. It can be seen that the pressure at the wall focuses with time, and is dominated by the swirl velocity for later times. This focusing of the pressure is precisely what is seen in experiments on the retreating side of a helicopter airframe (Kim & Komerath 1995; figure 1*b*). Note that the $*$ denote the pressure at time $t = 0^-$ and the pressure again instantaneously jumps from this condition to its unsteady value.

From the results presented here, the vortex contracts locally near the wall as is seen in experiments. Coincident with the contraction of the swirl velocity the suction peak grows in magnitude monotonically with increasing time. This result is a likely explanation for the lingering suction peak seen in experiments on the retreating side of the airframe (see figure 1). Note that for larger times, because of the rapid variation in the flow near $r = 0$, the numerical scheme becomes unstable and the solution breaks down. In practice, this will not occur because viscosity becomes important when fluid

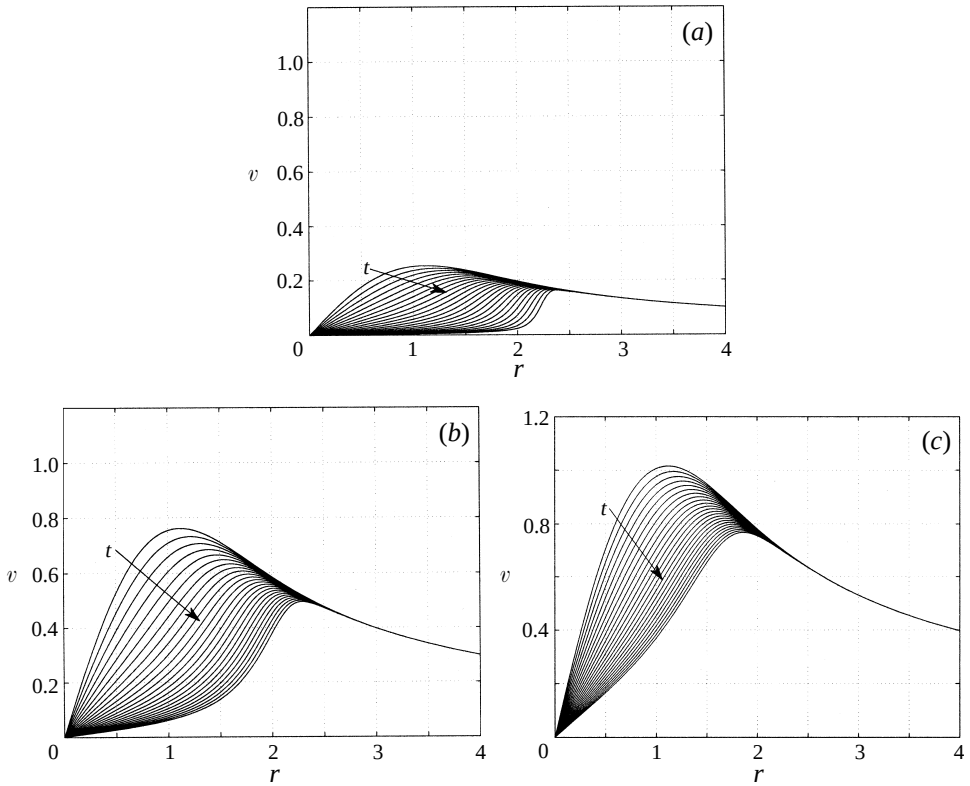

FIGURE 16. Swirl velocity on the wall for the vortex–jet with axial flow directed toward the wall for three values of Γ. (*a*) $\Gamma = 2.5$ for time ranging from 0 to 2.5 in increments of 0.1. (*b*) $\Gamma = 7.5$ with time ranging from 0 to 2.5 in increments of 0.1. (*c*) $\Gamma = 10$ with time ranging from 0 to 1.2 in increments of 0.05.

from the boundary layer is sucked into the vortex core thereby stemming the radial shrinking of the core.

6. The influence of circulation

In this section, the influence of the value of the circulation on the results for the case where the axial velocity in the vortex is directed toward the wall is discussed. In general, at small values of the circulation the flow behaves more like a jet, while at the larger values, the flow is dominated by the properties associated with a vortex, results which are to be expected.

Figure 16 shows the swirl velocity on the wall as a function of time for the three values of the circulation indicated. Note that the scales of the three figures are the same and the maximum azimuthal velocity rises linearly with circulation. Moreover, the rapid decrease in the azimuthal velocity occurs only very near the wall as shown on figure 17 for $\Gamma = 2.5$.

Figure 18 shows the axial vorticity on the wall. For each value of the circulation, the axial vorticity on the wall decreases near $r = 0$ as time increases, and spreads radially outward with time. It can be seen that the axial vorticity at the smaller values of the circulation first decreases at small r, but later increases as a shell of large

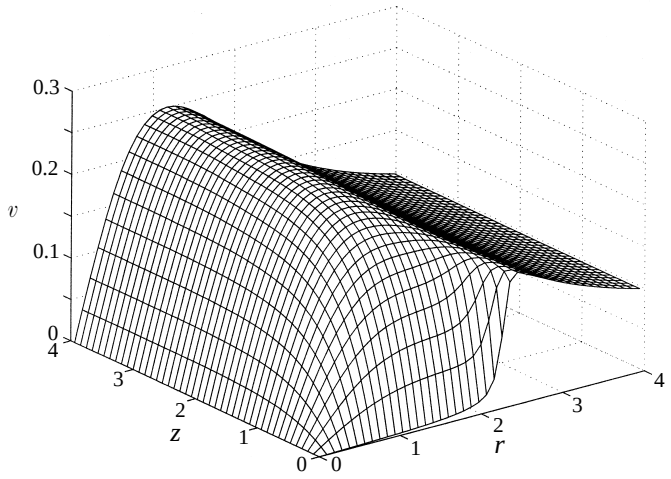

FIGURE 17. Swirl velocity field for the vortex–jet with axial flow directed toward the wall for $\Gamma = 2.5$ at time $t = 2.5$. Every third point is plotted.

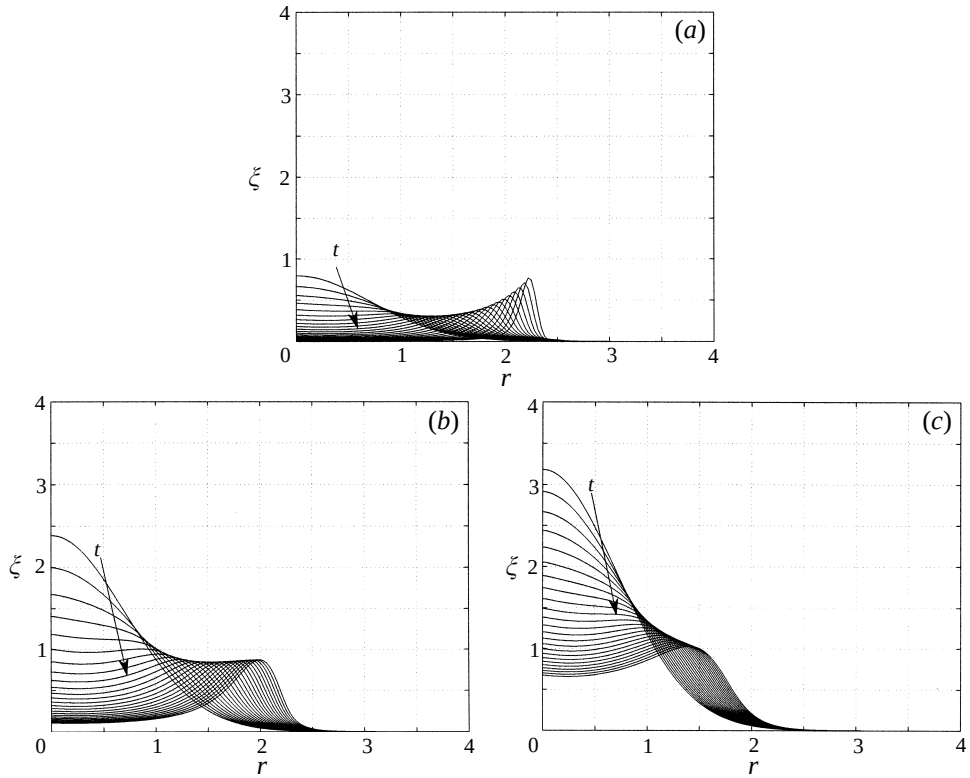

FIGURE 18. Axial vorticity on the wall for the vortex–jet with axial flow directed toward the wall for three values of Γ. (*a*) $\Gamma = 2.5$ for time ranging from 0 to 2.5 in increments of 0.1. (*b*) $\Gamma = 7.5$ with time ranging from 0 to 2.5 in increments of 0.1. (*c*) $\Gamma = 10$ with time ranging from 0 to 1.2 in increments of 0.05. Note the rapid decrease in the axial vorticity in the original core of the vortex.

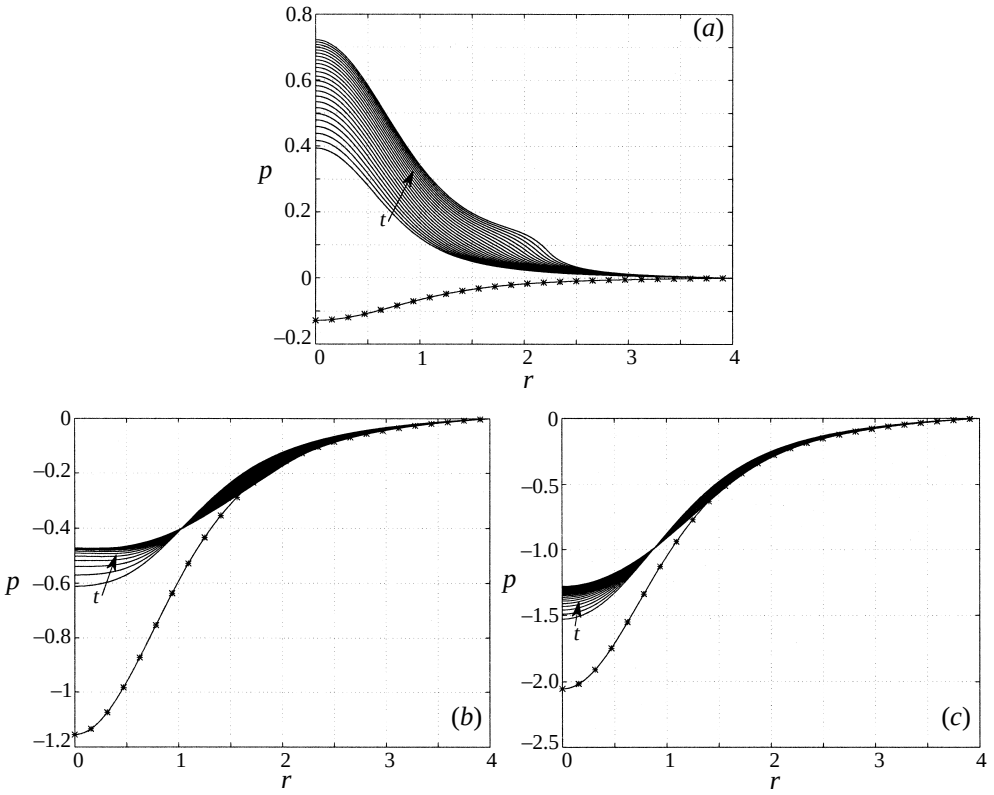

FIGURE 19. Pressure on the wall for the vortex–jet with axial flow directed toward the wall for three values of Γ. (*a*) $\Gamma = 2.5$ for time ranging from 0 to 2.5 in increments of 0.1. (*b*) $\Gamma = 7.5$ with time ranging from 0 to 2.5 in increments of 0.1. (*c*) $\Gamma = 10$ with time ranging from 0 to 1.2 in increments of 0.05. Note the rapid decrease in the pressure in the original core of the vortex. The $*$ indicate the initial condition, $t = 0^-$.

vorticity is formed. The results of figure 18(*c*) appear to be tending toward similar behaviour.

Figure 19 shows the pressure on the wall for each value of the circulation; again, the starred curve indicates the pressure at time $t = 0^-$ which is due to swirl only. For $\Gamma = 2.5$ the pressure actually rises above zero; that is, there is no suction peak associated with the pressure for this rather weak vortex. The results for the other values of the circulation are similar to that for $\Gamma = 5$. Note that for both $\Gamma = 7.5$ and 10, the pressure seems to approach a steady value near $r = 0$, as indicated by the clustering of curves at later times.

The azimuthal vorticity for each value of the circulation is shown on figure 20. For ease of comparison, the scale of the figure is chosen to be the same as the pure jet case, figure 7(*a*). Note that the azimuthal vorticity decreases substantially as the circulation increases. However, for the case of $\Gamma = 2.5$ the azimuthal vorticity is increasing in magnitude, as for the pure jet ($\Gamma = 0$) whereas for the other values, it is decreasing. The radial velocity (figure 21) shows similar trends.

Finally, it is of interest to examine the streamline patterns and compare those for the vortex–jet with those of the pure jet. Figure 22(*a*) presents the streamlines for the jet case at $t = 2.5$; the corresponding streamlines for the case of $\Gamma = 2.5$ at the same time are shown on figure 22(*b*). Note the similarity in the streamlines, which is

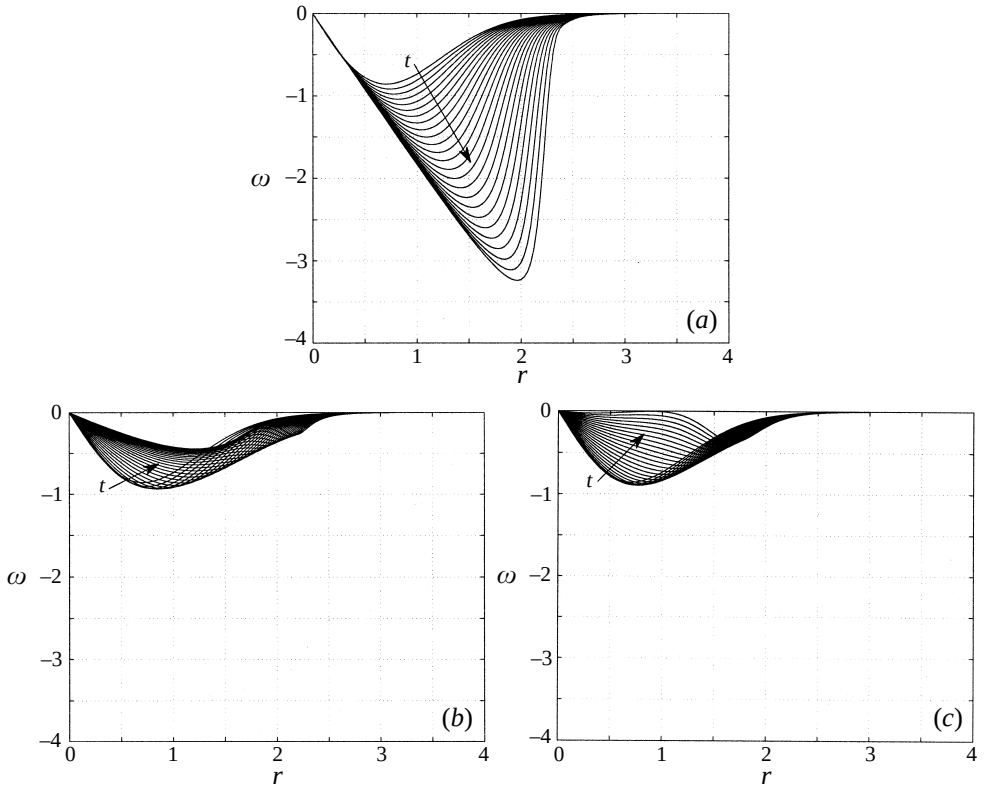

FIGURE 20. Azimuthal vorticity distribution on the wall for the vortex–jet with axial flow directed toward the wall for three values of Γ. (*a*) $\Gamma = 2.5$ for time ranging from 0 to 2.5 in increments of 0.1. (*b*) $\Gamma = 7.5$ with time ranging from 0 to 2.5 in increments of 0.1. (*c*) $\Gamma = 10$ with time ranging from 0 to 1.2 in increments of 0.05.

perhaps to be expected since the flow is assumed to be axisymmetric. On the other hand, it is surprising that they are so similar, although the streamlines near the wall persist closer to the axis for the vortex–jet. The streamlines are not substantially different at the higher values of the circulation.

For the larger values of the circulation (i.e. for $\Gamma = 7.5, 10$) and on the retreating side for $\Gamma = 2$ (and at the larger times), the computations were stopped when the radial velocity began to reverse direction near the plate. This 'separation' is believed to be a result of accumulated numerical error. In this region, the stream-function values are of the order of the discretization error in the equations; for all of the cases computed, reduction of the time step and the grid sizes considerably reduces the stream-function values. Another form of truncation-error-induced reversed flow can easily occur in the steady flow problem if not enough terms are taken in the series solution presented in the Appendix. The absence of reversed flow in the present work is counter to the conclusions of Marshall & Krishnamoorthy (1997) who show multiple eddies in their inviscid computation of a similar problem.

7. Comparison with experiment

While the present problem is an idealization of the situation where a tip vortex shed from a helicopter rotor blade strikes a circular cylinder, qualitative comparisons of the

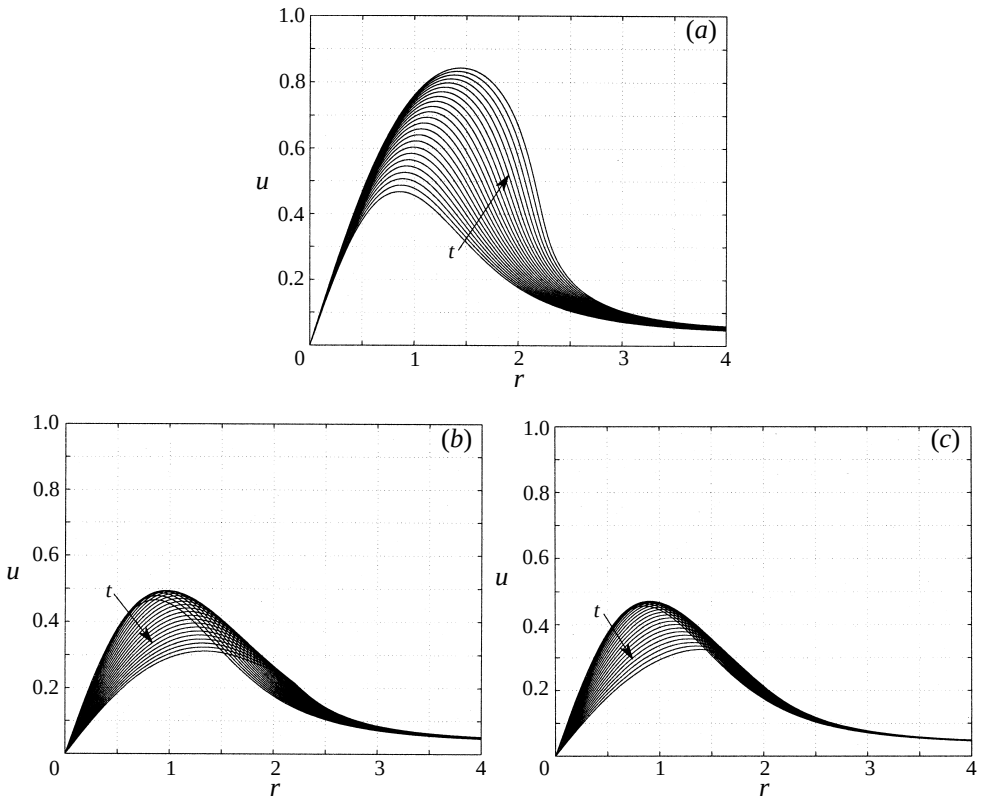

FIGURE 21. Radial velocity on the wall for the vortex–jet with axial flow directed toward the wall for three values of Γ. (*a*) $\Gamma = 2.5$ for time ranging from 0 to 2.5 in increments of 0.1. (*b*) $\Gamma = 7.5$ with time ranging from 0 to 2.5 in increments of 0.1. (*c*) $\Gamma = 10$ with time ranging from 0 to 1.2 in increments of 0.05.

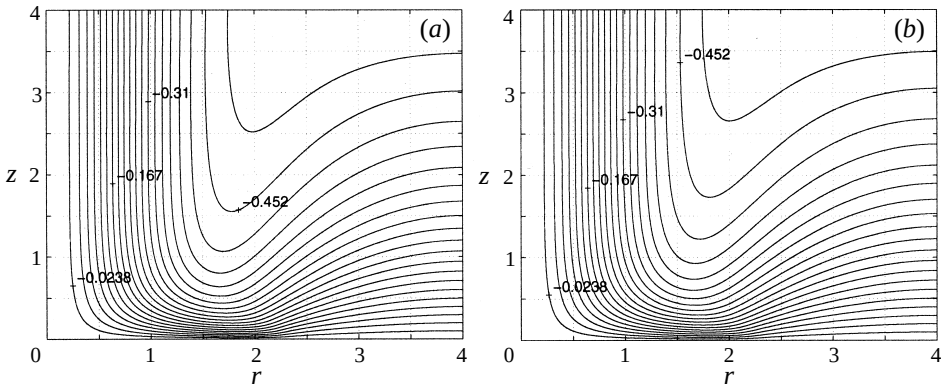

FIGURE 22. (*a*) Streamlines for jet flow at $t = 2.5$. (*b*) Streamlines for the vortex–jet with axial flow directed toward the wall ($\Gamma = 2.5$) at the same time. Note the similarity in the two plots.

time scale of the interaction may be made. From the non-dimensionalization in § 2, we can calculate the dimensional parameters in order to compare with experiments conducted by Kim & Komerath (1995). It is known from Kim & Komerath (1995) and a recent communication by R. Mahalingam (1996, personal communication)

that the nominal dimensional core radius is $a_v \sim 0.2$–0.4 in. The best estimates from experiment suggest that the maximum dimensional core velocity is $w_0 \sim 24\,\mathrm{m\,s^{-1}}$ at a rotor speed of 2100 r.p.m. Using a median value for the core radius of 0.3 in and $\Gamma^* \sim 1.5\,\mathrm{m^2\,s^{-1}}$ at 2100 r.p.m. (Affes *et al.* 1993) we have $\Gamma = 8.02$ for an axial flow of $24\,\mathrm{m\,s^{-1}}$.

From the numerical results presented for $\Gamma = 5$ in figure 9 it is seen that by the time $t = 2.0$, the swirl velocity in the core of the original vortex ($r \leqslant 1$) is reduced by more than one order of magnitude. This corresponds to a dimensional time of $t^* \sim 0.63$ ms. For $\Gamma = 7.5$ the results are similar. This is the same order of magnitude as the time frame for the reduction of the suction peak, as can be seen in figure 12. Data from the experiments show that the suction peak on the advancing blade side disappears in a time frame of $\Delta\Psi \sim 12^\circ$, where Ψ denotes rotor phase angle. For a rotor angular speed of 2100 r.p.m., this corresponds to 0.95 ms. which is near the calculated value of 0.63 ms. Of course, the problem is much more complex than is considered here and so it is not expected that these parameters will exactly represent what is happening in the experiments. Nevertheless the fact that the computational time scale of the interaction on the advancing blade side compares favourably with the time scale in the experiment is encouraging.

8. Discussion

In the present paper we have calculated the inviscid response of a vortex to the presence of a wall and compared these results to the case of a jet. Initially, the wall is absent and is then suddenly inserted at time $t = 0$. This process is analogous to that which occurs in the impingement of a tip vortex on a helicopter airframe. The evolution of the vortex for times $t > 0$ for initial conditions corresponding to a Lamb vortex has been calculated. For axial flow in the vortex directed toward the wall, the vortex core is seen to 'bulge' as indicated by the radial convection of the point of maximum swirl velocity as depicted on figure 9(*a*), for example. The swirl velocity decreases rapidly in the core of the vortex allowing the pressure distribution to return to its steady-state, mean value as observed in experiments. The time scale associated with the reduction of the pressure spike depends on the magnitude of the axial velocity in the core of the vortex and on the nominal vortex core radius. At the same time the axial vorticity near the axis decreases by an order of magnitude with a consequent increase at larger radii as the vorticity is carried outward by the induced radial velocity. A similar comment applies to the azimuthal vorticity.

For the case where the axial flow is directed away from the wall, the axial vorticity is redistributed inward and the vortex core radius shrinks. At the same time the suction peak increases in amplitude and focuses. The essential features of the process described here have been observed on the advancing side of the helicopter rotor in experiments (Kim & Komerath 1995). The present results suggest that as the vortex travels down the airframe, its profile will look something like that depicted on figure 23. An analytical solution also was obtained for the swirl case and the results compare very well with the computational results (figure 4).

What is surprising in the present work is that the jet produces similar trends with regard to the streamline patterns; i.e. the streamline patterns are qualitatively independent of swirl. The azimuthal vorticity, initially concentrated near the wall, is convected outward into the irrotational outer region, forming a wave front of vorticity which steepens as time increases. The numerical solution indicates a trough in the streamlines (figure 22), which moves outward in time roughly at the same

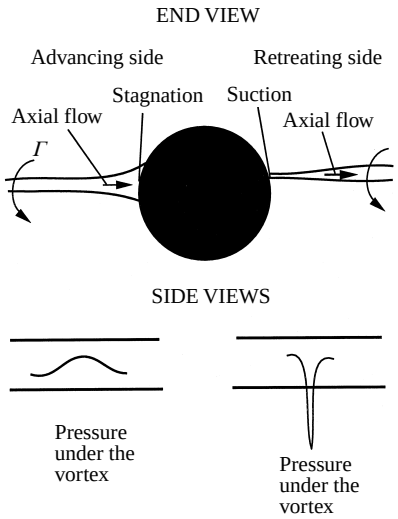

FIGURE 23. A sketch of the tip-vortex structure along the sides of the airframe as described by Kim & Komerath (1995) and the present results. The pressure under the vortex along the sides of the airframe is also shown. The core radius of the vortex is greatly enlarged for clarity. Arrows denote direction of axial flow within the vortex.

speed as the peak of the azimuthal vorticity. This trough corresponds to the change of sign of velocity normal to the wall that is predicted by the analytical solution for $t = 0^+$ (§ A.1). In the no-swirl case, the results of the time-marching computation tend toward the steady-state solution (§ A.2), for which azimuthal vorticity of the form $\omega = rH(\Psi)$ satisfies the conservation equation (11), where H is a function defined by the values of Ψ and ω at the inflow boundary. At the surface, this functional form produces vorticity whose magnitude grows linearly with r. This analytical solution, corresponding to conditions after the vorticity wave front has passed, predicts a layer of vorticity next to the surface which thins with increasing radius, thus concentrating the vorticity in ever greater levels.

A central suction peak is exhibited by the wall-pressure results for sufficiently large swirl. The magnitude of this suction peak diminishes rapidly at a rate depending on the value of circulation. The results indicate that the pressure approaches a steady-state distribution, and that an order-of-magnitude decrease in the amplitude of the pressure spike can occur very quickly for large values of circulation.

The fact that the dominant physics of the present problem is inviscid is not as surprising as it may seem. The induced pressure on the airframe is intimately related to the vorticity field through the local velocity field. Consider the situation where the ratio of the vortex core radius to the characteristic body length scale is small but finite and the case of a strong vortex in the sense that the dimensionless circulation based on free-stream variables $\Gamma = \Gamma^*/W_\infty a$, where a is the body length scale, is $O(1)$. Then the vortex Reynolds number, $Re_v = \Gamma^*/\nu$ is the same order of magnitude as the Reynolds number based on the body length scale and the external mean velocity, W_∞, i.e. $Re = W_\infty a/\nu$. Assuming that the scaled vortex radius in laminar flow is $O(Re^{-1/2})$, then from a simple Rankine vortex model the swirl velocity is $O(Re^{1/2})$. Since the axial vorticity is essentially the radial derivative of the swirl, it is easily seen that the axial vorticity within the vortex core is of magnitude $\xi \sim Re$ (see equation (6)). If the axial velocity within the vortex is of the same order as the

swirl, then similarly, the azimuthal vorticity is $\omega \sim O(Re)$. The vorticity magnitude within a classical laminar boundary layer on the body is $O(Re^{1/2})$ and so the vorticity within the vortex is much larger than that in the boundary layer. In particular, it is expected that in the collision process the magnitude of the vorticity field within the vortex will be reduced to the order of magnitude of the boundary layer vorticity, in which case distinguishing between boundary layer and vortex vorticity becomes impossible. This is the essence of the vorticity redistribution process; vorticity is not destroyed but merely redistributed in an inviscid way. As is well known, this is a major computational simplification: the dominant features of the collision process need not be modelled using the full Navier–Stokes equations. Coinciding with this redistribution of vorticity is the relaxation or focusing of the pressure suction peak associated with the original vortex. In this regard, it is useful to note that for small circulation when the boundary layer and vortex vorticity are of the same order (i.e. a weak vortex) the interaction between the vortex and the boundary layer is very weak. The same ideas may be applied to three-dimensional vortex sheets which in the present application are much weaker and thus much more benign in terms of impulsive loading on the airframe.

Viscous effects must become important in the case where the core axial velocity is away from the wall. The phenomenon of viscous limiting of vortex core thinning is suggested in studies by Burggraf & Stewartson (1971), who investigated the boundary layer induced by a potential vortex oriented normal to a coaxial disc. Their results showed that the radial inflow in the boundary layer induced by the vortex will erupt from the wall at $r = 0$, continually feeding the core, and thereby halt the focusing of the swirl velocity seen in the present results. Incorporation of the boundary layer in the present vortex model may provide additional fluid so that the vortex can persist for a long period of time (figure 1*b*); otherwise, it is evident from the present results that the swirl velocity focuses and this process cannot continue indefinitely in an inviscid fluid.

This work has been supported by the US Army Research Office under grant DAAH04-93-G-0048. The continued support of the contract monitor Dr Thomas L. Doligalski is greatly appreciated. The computations have been performed through a grant of computer time from The Ohio Supercomputer Center. The authors would like to express their gratitude to the referees for their helpful comments which have led to an improved paper.

Appendix. Analytical solutions for a Gaussian jet

In this Appendix we present analytical solutions for the initial and terminal states of flow for the Gaussian jet, defined in equation (29). The analysis below makes use of normalized variables, so that r implies r/a, w implies w/w_0, etc. For axisymmetric incompressible flow, the stream function Ψ must satisfy equation (9). The difference in the two limit cases is the form that the vorticity must take.

A.1. *Starting solution:* $t = 0^+$

Initially the vorticity is that of the undisturbed jet, given by equation (33) for the Gaussian jet. The stream function is governed by equation (9), which for this case may be expressed in the form

$$4\rho\frac{\partial^2\Psi}{\partial\rho^2} + \frac{\partial^2\Psi}{\partial z^2} = 2\rho\,\mathrm{e}^{-\rho}$$

where we have utilized the variable $\rho = r^2$. The stream function distribution for the undisturbed jet provides a particular solution of this equation

$$\Psi^{(0)} = -\tfrac{1}{2}\left(1 - \mathrm{e}^{-r^2}\right). \tag{A 1}$$

A complementary function, satisfying the homogeneous equation, must be added to satisfy the boundary condition $w = 0$ at the surface $z = 0$. Omitting the details, we observe that the complementary function can be expressed as a Fourier–Bessel integral, so that the complete solution has the form

$$\Psi = \frac{1}{2}\left\{-\left(1 - \mathrm{e}^{-r^2}\right) + r\int_0^\infty J_1(\lambda r)\mathrm{e}^{-\lambda z - \lambda^2/4}\mathrm{d}\lambda\right\}. \tag{A 2}$$

The velocity components can now be evaluated from the partial derivatives of Ψ. In particular the surface velocity has the form

$$u(r,0) = \frac{1}{2}\int_0^\infty \lambda J_1(\lambda r)\mathrm{e}^{-\lambda^2/4}\mathrm{d}\lambda.$$

This integral has been evaluated in terms of the modified Bessel functions (Erdelyi *et al.* 1954). There results

$$u(r,0) = \frac{\pi^{1/2}}{2} r\,\mathrm{e}^{-r^2/2}\left[I_0(r^2/2) - I_1(r^2/2)\right]. \tag{A 3}$$

An interesting feature of the flow is the sign of the axial velocity near the wall. From the continuity equation, the derivative $\partial w/\partial z$ also can be evaluated in terms of modified Bessel functions:

$$\left.\frac{\partial w}{\partial z}\right|_{z=0} = -\left.\frac{1}{r}\frac{\partial(ur)}{\partial r}\right|_{z=0} = -\pi^{1/2}\mathrm{e}^{-r^2/2}\left[(1-r^2)I_0(r^2/2) + r^2 I_1(r^2/2)\right]. \tag{A 4}$$

This expression has a zero at the radius $r^* = 1.256\,963\cdots$, so that the flow is toward the wall for $r < r^*$ and away from the wall for $r > r^*$.

A.2. *Steady state: $t \to \infty$*

We now consider the terminal state of steady flow. The conservation laws for axisymmetric flow require ω/r to be constant on streamlines, so that we can write

$$\omega = rH(\Psi). \tag{A 5}$$

The stream function Ψ still satisfies equation (9), which now takes the special form

$$\mathrm{D}^2\Psi = -r^2 H(\Psi). \tag{A 6}$$

The azimuthal vorticity in the undisturbed jet at upstream infinity is given by equation (33). Making use of equation (A 1), we find that the function $H(\Psi)$ has the form

$$H(\Psi) = -2(1 + 2\Psi). \tag{A 7}$$

$H(\Psi)$ is invariant throughout the flow field. Hence equation (A 6) simplifies to a linear partial differential equation:

$$\mathrm{D}^2\Psi - 4r^2\Psi = 2r^2. \tag{A 8}$$

A particular solution of this equation is given by (A 1). The homogeneous equation can be solved readily by the method of separation of variables, leading to the complete

solution in the form of a series of associated Laguerre polynomials, as

$$\Psi = -\tfrac{1}{2}\left(1 - \mathrm{e}^{-r^2}\right) + r^2\,\mathrm{e}^{-r^2}\sum_{n=0}^{\infty} c_n\, L_n^1(2r^2)\,\mathrm{e}^{-(8(n+1))^{1/2}z}. \tag{A 9}$$

The exponentially growing solution has been suppressed, so that the flow predicted by (A 9) approaches that of (A 1) as $z \to \infty$. Also Ψ automatically vanishes for $r = 0$ and $r \to \infty$, leaving only the boundary condition at the wall, $z = 0$, to be satisfied. Set $z = 0$ in equation (A 9), and multiply through by $\mathrm{e}^{-r^2} L_m^1(2r^2)$. Then integrating from $r = 0$ to ∞, the orthogonality of the Laguerre polynomials leads to the following set of equations for the coefficients:

$$c_n = \frac{4}{n+1}\int_0^{\infty} \mathrm{e}^{-r^2}(1 - \mathrm{e}^{-r^2})\, L_n^1(2r^2)\, r\mathrm{d}r.$$

These integrals may be evaluated using the generating function for L_n^1, yielding the simple result

$$c_n = \frac{(-1)^n}{n+1}.$$

Owing to the exponential factor, the series in equation (A 9) converges fairly rapidly except near $z = 0$. On $z = 0$, the terms decay like $(-1)^n n^{-1/2}$ for large n, except at $r = 0$, where even slower convergence occurs. However, if one evaluates the Laguerre polynomials successively using their recurrence relation, term-by-term summation on a desk-top computer requires only a few seconds for a given point located near both wall and axis.

The velocity components u and w (radial and axial) are obtained as derivatives of the stream function, as

$$u = -\frac{1}{r}\frac{\partial \Psi}{\partial z}, \quad w = \frac{1}{r}\frac{\partial \Psi}{\partial r}.$$

Thus we find for the surface velocity

$$u(r, 0) = r\,\mathrm{e}^{-r^2}\sum_{n=0}^{\infty} c_n\,(8(n+1))^{1/2}\, L_n^1(2r^2)$$

and for the axial velocity

$$w(0, z) = -1 + 2\sum_{n=0}^{\infty} c_n\, L_n^1(0)\,\mathrm{e}^{-(8(n+1))^{1/2}z}.$$

The axial velocity series for $w(0, z)$ converges except at the wall, $z = 0$. However, we know that w must vanish on $z = 0$, since the stream function does. Above the surface the radial velocity series converges owing to the exponential factor, although we have not written down its explicit form. The surface velocity series, however, is an oscillatory (though not alternating) series converging slowly with terms decaying as $n^{-1/4}, r > 0$. Note that the Euler transformation (Bromwich 1949) can be used to dramatically accelerate convergence of the axial-velocity series, even at the wall, but this technique is not successful for the surface velocity.

The azimuthal vorticity takes an especially simple form on the wall. From equations (A 5) and (A 7), we find

$$\omega = rH(0) = -2r$$

so that the magnitude of the vorticity simply increases linearly with radius. It is

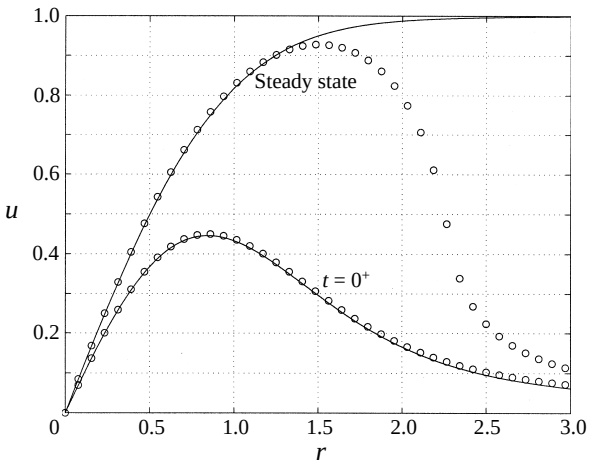

FIGURE 24. Radial velocity on the surface for the starting solution, $t = 0^+$, and for the terminal steady flow, $t \to \infty$. The open circles are the numerical solution, with the solid line being the analytical solution. The numerical solution is evaluated at $t = 2.5$ and at $t = \Delta t = 0.005$. The numerical solution for times in between is given in figure 6.

interesting that this result is obtained *ab initio*, without resort to the solution of the differential equation.

We also note that the solution may be expanded in terms of the similarity variable $\eta = rz$. There results for the radial velocity, for example,

$$u(r, z) \sim \mathrm{e}^{-2\eta} + \frac{1}{6r^4}\eta^2(2\eta - 3)\mathrm{e}^{-2\eta}.$$

Hence the velocity decays exponentially to zero for any positive fixed value of z, except within a layer of order $z \sim 1/r$ next to the wall.

A.3. *Results*

The flow speed at the surface is plotted in figure 24 for the starting solution, $t = 0^+$, and for the terminal steady flow, $t \to \infty$. For the starting solution, the surface speed peaks at the value 0.445 82 at the radius $r = 0.844\,23$; i.e. 45% of the peak speed in the undisturbed jet at 84% of the characteristic radius of the jet. For large radii, $u(r, 0)$ decays as $1/2r^2$.

For the steady-flow case, the series for Ψ, equation (A 9), was summed at discrete points above the wall. Forward differences were applied to the resulting numerical data to obtain the z-derivative needed for the radial velocity. The results were deemed sufficiently accurate when values obtained from difference formulas of both third-order and fourth-order accuracy agreed to five significant figures. This test corresponded to six-place accuracy in the stream-function sums. The results are also shown in figure 24. The surface flow speed for steady flow increases monotonically with radius, rapidly approaching the maximum speed of the original undisturbed jet, as required by conservation of total pressure on the central streamline.

REFERENCES

AFFES, H., CONLISK, A. T., KIM, J. M. & KOMERATH, N. M. 1993 A model for rotor tip vortex-airframe interaction, Part 2: Comparison with experiment. *AIAA J.* **31**, 2274–2282.

BATCHELOR, G. K. 1964 Axial flow in trailing line vortices. *J. Fluid Mech.* **20**, 645–658.

Brand, A. G., McMahon, H. M. & Komerath, N. M. 1990 Correlations of rotor/wake-airframe interaction measurements with flow visualization data. *Annual Forum Proceedings, American Helicopter Society*, vol. 2, pp. 1135–1143.

Bromwich, T. J. I'a. 1949 *An Introduction to the Theory of Infinite Series*, 2nd Edn, Revised, p. 62. MacMillan.

Burggraf, O. R. & Stewartson, K. 1971 Boundary layer induced by a potential vortex. *Phys. Fluids* **14**, 1821–1833.

Conlisk, A. T. 1997 Modern helicopter aerodynamics. *Ann. Rev. Fluid Mech.* **27**, 515–567.

Erdelyi, A., Magnus, W., Oberhettinger, F. & Tricomi, F. G. 1954 *Tables of Integral Transforms*, vol. II, p. 29. McGraw Hill.

Kim, J. M. & Komerath, N. M. 1995 Summary of the interaction of a rotor wake with a circular cylinder. *AIAA J.* **33**, 470–478.

Lamb, H. 1945 *Hydrodynamics*, 6th Edn, p. 592. Dover.

Lee, J. A., Xiao, Z., Burggraf, O. R., Conlisk, A. T. & Komerath, N. M. 1995 An inviscid analysis of vortex/surface collisions. *AIAA Paper* 95-2237.

Liou, S. G., Komerath, N. M. & McMahon, N. M. 1990 Measurement of the interaction between a rotor tip vortex and a cylinder. *AIAA J.* **28**, 975–981.

Marshall, J. S. & Krishnamoorthy, S. 1997 On the instantaneous cutting of a columnar vortex with non-zero axial flow. *J. Fluid Mech.* **351**, 41–74.

Marshall, J. S. & Yalamanchili, R. 1994 Vortex cutting by a blade. Part II. Computations of the vortex response. *AIAA J.* **32**, 1428–1436.

McCroskey, W. J. 1995 Vortex wakes of rotorcraft. *AIAA Paper* 95-0530.

Rockwell, D. 1983 Oscillations of impinging shear layers. *AIAA J.* **21**, 645–664.

Rockwell, D. 1998 Vortex-body interactions. *Ann. Rev. Fluid Mech.* **28**, 199–229.

Rockwell, D. & Naudascher, E. 1979 Self-sustained oscillation of impinging shear layers. *Ann. Rev. Fluid Mech.* **11**, 67–94.

Saffman, P. G. & Baker, G. R. 1979 Vortex interactions. *Ann. Rev. Fluid Mech.* **11**, 95–122.

Sarpkaya, T. 1989 Computational methods with vortices – The 1988 Freeman Scholar Lecture. *Trans. ASME*: I *J. Fluids Engng* **111**, 5–52.

Smith, G. D. 1985 *Numerical Solution of Partial Differential Equations: Finite Difference Methods.* Oxford University Press.

Tucker, B. & Conlisk, A. T. 1992 Massive vortex motion in the presence of solid boundaries. *Phys. Fluids* **4**, 290–305.

Yu, Y. H. 1995 Rotor blade vortex interaction noise: generating mechanisms and its control concepts. *American Helicopter Society Specialists' meeting on Aeromechanics Technology and Product Design, Bridgeport CT, October 11–13, 1995.*